energies

MDPI

Article

Falling Film Flow and Heat Transfer of Cryogenic Liquid Oxygen on Different Structural Surfaces

Zhihua Wan [1,*], Ping Wang [1], Huanying Shen [2] and Yanzhong Li [3]

[1] School of Energy and Mechanical Engineering, Jiangxi University of Science and Technology, Nanchang 330013, China; pingwang@jxust.edu.cn
[2] Institute of Building Intelligence, Jiangsu Vocational Institute of Architectural Technology, Xuzhou 221116, China; hyshen1125@163.com
[3] Institute of Refrigeration and Cryogenic Engineering, Xi'an Jiaotong University, Xi'an 710049, China; yzli-epe@mail.xjtu.edu.cn
* Correspondence: zhwan@jxust.edu.cn

Abstract: The accurate prediction of the falling film characteristics of cryogenic liquids is necessary to ensure good evaporation performance, due to their special physical properties. In this study, the film flow and heat transfer characteristics on four different structures were investigated, and the performance of the cryogenic liquid oxygen was compared with other fluids with higher temperatures, which demonstrates the influence of structures and liquid mediums. The VOF model was used to capture the film surface in the simulation model. The results show that for the four structures, liquids with higher kinematic viscosity tend to have greater film thickness, and the sensible heat transfer coefficients are inversely related to the nominal thermal resistance of falling film flow. Both on the smooth plate and the corrugated plate, the film wettability depends on the kinematic viscosity, rather than the dynamic viscosity, and the effect of kinematic viscosity is greater than that of surface tension. Both the local heat transfer coefficient and its fluctuation amplitude decrease gradually along the flow direction on the triangular corrugated plate, and the vortices are easier to produce at the wall troughs when the film viscosity is higher. At the bottom of the horizontal tube, the increases in local film thickness of the liquid oxygen are less than those of the water and the seawater. More liquid tends to accumulate at the bottom of the round tube, while it easily detaches from the film surface of the elliptical tube. For the horizontal tubes, the local heat transfer coefficients decrease rapidly when θ = 0–5°, and increase sharply at θ = 175–180°.

Keywords: falling film; elliptical tube; VOF; film thickness; heat transfer; simulation

Citation: Wan, Z.; Wang, P.; Shen, H.; Li, Y. Falling Film Flow and Heat Transfer of Cryogenic Liquid Oxygen on Different Structural Surfaces. *Energies* **2022**, *15*, 5040. https://doi.org/10.3390/en15145040

Academic Editors: Pavel Skripov and Aleksandr Pavlenko

Received: 14 May 2022
Accepted: 5 July 2022
Published: 10 July 2022

1. Introduction

Falling film technology has the advantages of low pressure drop, high heat and mass transfer, small liquid charge, which has been widely used in many fields such as desalination, refrigeration, chemical processes. The structures for the falling film evaporators include plates, tubes, packed columns and so on [1–4]. The falling film evaporators contribute to energy saving, while there are many factors influence on the heat and mass transfer performance. Therefore, a large amount of attention has been paid to these fields.

Horizontal tubes are often chosen as the structure type of falling film evaporators in the desalination and refrigeration fields. John et al. [5] compared the performance of eight liquid distributors for the film flow over horizontal tube banks. By using the chromatic confocal displacement sensor, Chen et al. [6] measured the film thickness on the horizontal tube under the droplet and sheet flow. Chen et al. [7] proposed a correlation to predict the flow pattern transitions over enhanced tubes with 2D integral fins based on the experimental data. Zheng et al. [8] studied periodical film fluctuation characteristics over a superhydrophilic tube, and the wall temperature was monitored by the infrared

camera. Hong et al. [9] measured the heat transfer coefficients of R134a film flow on the surface-modified tubes.

With the CFD method, Cao et al. [10] acquired that finned tubes can influence on the film spreading. Zhang et al. [11] simulated the effect of gas flow on the film thickness distribution. Guo et al. [12] investigated the film flow on the horizontal round tube under column flow, the film thickness and heat transfer coefficients along the axial direction were acquired. Zhao et al. [13] numerically studied the effect of the tube bundle arrangement on the film flow and heat transfer. Karmakar et al. [14] explored the sensible heat transfer coefficients of falling film on the horizontal tube under different flow patterns, namely, the droplet, jet, and sheet regimes. The sensible heat transfer is a common term used in the heat transfer field, which means only temperature variation of liquid film happens under this heat transfer process without phase change. Mao et al. [15,16] simulated the heat recycles from the oily wastewater film by falling on a horizontal tube, and the effects of oil content, tube diameter, spray density on heat transfer were analyzed. Tahir et al. [17] set up a numerical model to calculate the film flow of LiBr-H_2O solution on the horizontal tube, and the effects of the liquid load and the concentration on the film hydrodynamics were examined. In addition, the falling film absorber using horizontal tubes was theoretically modelled with an aqueous alkaline nitrate solution as working fluid [18].

For film flow on the vertical walls, Huang et al. [19] explored the film evaporation and sensible heat transfer inside the converging-diverging tubes, and found the rid height has great impact on the heat transfer performance. Eichinger et al. [20] studied that the R290 film flow inside a vertical round tube, and showed the groove structure improves the wetting behavior and heat transfer. Wang et al. [21] measured the film thickness on the vertical plate by the confocal chromatic technique, a film thickness correlation was proposed for the ionic liquids.Li et al. [22] numerically studied the film flow outside the vertical tube, and found the ripple surface structure hinders the film spreading, which results in smaller velocity and greater film thickness compared with the smooth tube. Jourdan et al. [23] investigated the wettability and film thickness on the cooling tower packing by the fluorescence method. Shi et al. [24] obtained the film thickness of the falling film absorption by the optical method, and found the waviness intensity contributes to the mass transfer rate. Wei et al. [25] defined the minimum wetting rate (MWR) when the film firstly wets the wall completely as the mass flow increases, and explored the effect of the groove structure and the contact angle on the MWR.

The working fluids studied in the existing literature are mainly concentrated in pure water [5–8,10,11,13,19,23,25], seawater [3], oil sewage [15,16], LiBr solution [17], freon refrigerant [9,20,22], ethylene glycol aqueous solution [14], potassium formate aqueous solution [24], ionic fluid [21,22]. For the cryogenic liquid, Pavlenko et al. [26] measured the film flow of cryogenic liquid nitrogen on the surfaces with complex geometry, and found the microstructure has a significant influence on the film spreading progress. Zhou et al. [27] adopted the mathematical model to analyze film flow in the plate-fin condenser/reboilers of air separation, in which liquid oxygen evaporates and gas nitrogen condensates.

In summary, Gu et al. [28] pointed out the cryogenic liquid oxygen has special physical properties such as low viscosity and surface tension, which is quite different from common fluids under room temperature. In addition, the cryogenic experiment has deficiencies of high cost and large measurement error. Therefore, the numerical method is particularly suitable to study the falling film characteristics of cryogenic liquids. At present, there is not too much research focused on the film flow characteristics of cryogenic liquid oxygen, especially on the horizontal tubes, which is still necessary to explore in depth. In the present study, four typical working fluids and four different structures are selected to simulate the effects of physical properties and wall structures on the falling film characteristics. In the following, the mathematical models and numerical implementation are described firstly, and the Fluent 18.0 software is adopted to simulate the falling film process. Through comparing results of falling film flow, wettability and heat transfer characteristics under

four structures, and some useful conclusions are drawn finally, which contributes to the design of falling film evaporators.

2. CFD Model

2.1. Physical Models and Boundary Conditions

Four different structures, namely a smooth plate, triangular corrugated plate, round tube, and elliptical tube, are studied in the present study. As shown in Figure 1a, the dimensions (length L × depth D) of the 2D smooth plate are 60 mm × 4 mm, and the depth for the liquid inlet is 0.4 mm. Figure 1b depicts the 3D smooth plate, whose dimensions (length L × depth D × width W) are 60 mm× 7 mm× 50 mm, and the liquid inlet is also 0.4 mm in depth. Figure 1c,d show the 2D and 3D triangular corrugated plates, and their plate dimensions, including the length L, depth D, and width W, which are equal to those in the corresponding smooth plates. The only difference is in the bottom wall. For the 2D model, the dimensions of the triangular unit are Le = 5 mm and De = 0.7 mm. For the 3D model, the dimensions of the triangular unit are Le = 6 mm and De = 0.6 mm. To reduce the calculation cost, only half models are set up for the 3D models of the smooth plate and the triangular corrugated plate. The coordinates x, y, and z represent the width, length, and depth directions, respectively. The inclination angle ϕ is defined as the angle between the bottom wall and the horizontal ground. As for the horizontal tube, Figure 1e depicts the physical model of one half round tube. The tube diameter and the liquid inlet length are 60 mm and 1 mm, respectively. Figure 1f shows the elliptical tube model, whose tube perimeter P_t and ellipticity E are 62.8 mm and 2.5, respectively. The peripheral angle θ is defined as the angle starting from the tube top to the tube bottom.

The 2D models of the smooth plate, the triangular corrugated plate, the round tube, and the elliptical pipe were used to simulate the film flow and heat transfer characteristics, and the 3D plate models were used to simulate the film wettability. Mesh independency studies were conducted for all the models. For example, we established three mesh models with grid numbers of 6438, 10,360, and 16,591 for the 2D smooth plate, and acquired the average heat transfer of h_{ave} = 3437, 3465, and 3470 $W \cdot m^{-2} \cdot K^{-1}$, respectively, at Re = 1200, φ = 90°. Then the mesh model with 16,591 grid numbers was chosen as the final calculation model. The velocity inlet was employed both in the liquid inlet and the gas inlet boundary. The outlet and the walls were set as the pressure outlet and the no-slip wall conditions, respectively. In the present study, a wall with a constant contact angle of 70° was applied to acquire the film wettability under this condition. The remaining boundaries were all set as the symmetry condition. Other detailed numerical settings can be found in [2–4].

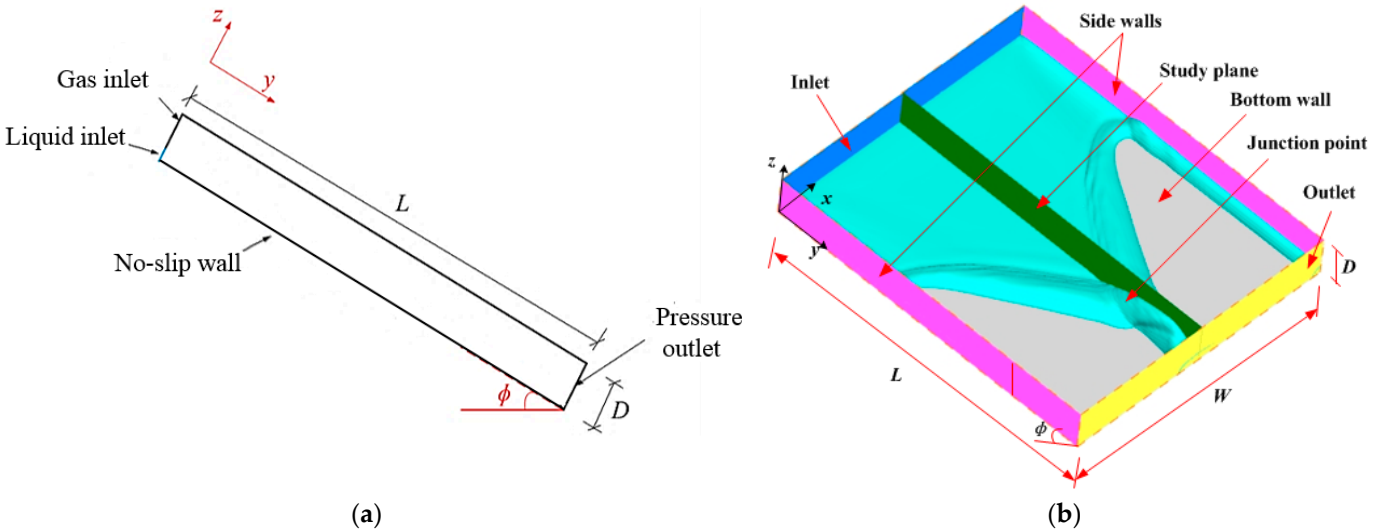

Figure 1. *Cont.*

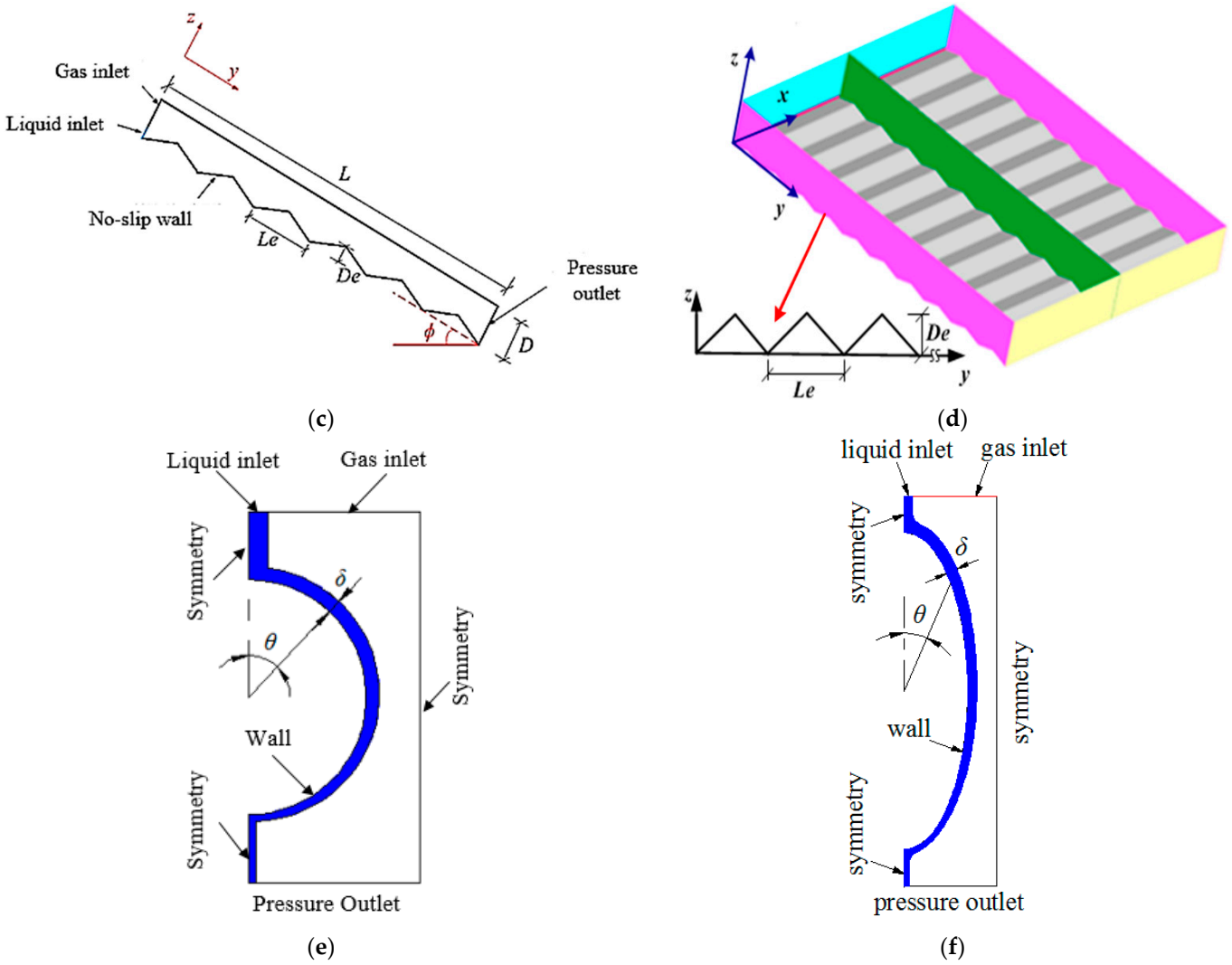

Figure 1. The physical models of different structures: (**a**) 2D smooth plate; (**b**) 3D smooth plate; (**c**) 2D triangular corrugated plate; (**d**) 3D triangular corrugated plate; (**e**) round tube; and (**f**) elliptical tube.

2.2. Assumptions and Mathematical Models

In order to simplify the calculation models, some assumptions were made as below: (1) all the liquid and gas phases were treated as incompressible fluids with constant properties; (2) the flow regime was laminar flow; (3) the shear force upon the gas–liquid interface was ignored; and (4) only sensible heat transfer happened during the heat transfer process. The general governing equations are given as below:

$$\nabla \cdot (\vec{v}) = 0 \tag{1}$$

$$\frac{\partial}{\partial t}\left(\rho \vec{v}\right) + \nabla \cdot \left(\rho \vec{v} \vec{v}\right) = -\nabla p + \mu \nabla^2 \vec{v} + \rho \vec{g} + \vec{F}_{\text{vol}}. \tag{2}$$

$$\frac{\partial (\rho T)}{\partial t} + \nabla \cdot (\rho \vec{v} T) = \nabla \cdot (\frac{\lambda}{c_p} \nabla T) \tag{3}$$

where $\vec{v}$ represents the velocity vector and $\vec{F}_{\text{vol}}$ refers to the volume force in the momentum conservation equation. In the present study, the surface tension is added into the

volume force, which is based on the continuum surface force (CSF) model proposed by Brackbill et al. [29]:

$$\vec{F}_{\mathrm{vol}} = \sigma_{lg} \frac{\alpha_l \rho_l \kappa_g \nabla \alpha_g + \alpha_g \rho_g \kappa_l \nabla \alpha_l}{0.5(\rho_l + \rho_g)} \tag{4}$$

where κ_l ($\kappa_l = \nabla \cdot (\nabla \alpha_l / |\nabla \alpha_l|)$) and κ_g ($\kappa_g = \nabla \cdot (\nabla \alpha_g / |\nabla \alpha_g|)$) refer to the curvature of the liquid and gas surfaces, respectively. σ_{lg} refers to the surface tension coefficient of the gas–liquid interface.

The film surface is tracked by solving the conservation equation of the volume fraction in Equation (5):

$$\frac{\partial \alpha}{\partial t} + \vec{v} \cdot \nabla \alpha = 0 \tag{5}$$

where α is the volume fractions of the liquid and gas phase, and they sum to achieve unity in each cell.

The Reynolds number (*Re*) is defined as $Re = 4\Gamma/\mu_l$, where Γ represents the film mass flow rate per unit length, and μ_l represents the liquid dynamic viscosity. For the vertical film flow, it is found that the film regime is laminar at $Re \leq 1600$ [30]. Moreover, the film surface is smooth and laminar near the region of liquid inlet, which is defined as the wave inception [31,32]. Furthermore, we acquired the length of wave inception at $Re = 1600$, for the water was less than 20 cm (see Figure 3 in [32]). In the present study, because the plate length is only 60 mm and the simulation *Re* is below 1600, thus, we chose the laminar model to simulate the film flow on the inclined plates. For the film on the horizontal tube, we acquired the film flow pattern of the present studied fluids in sheet flow at $Re \geq 634$, based on Equation (6), which is defined as the critical *Re* for the jet–sheet flow transition [33]. Moreover, it was measured that the laminar film conditions exist up to a film Reynolds number of about 2000 [34]. Therefore, we chose $Re = 2000$ as the studied condition to ensure the film situates at both the laminar flow and sheet flow.

$$Re = 1.448 Ga^{0.236} \tag{6}$$

where *Ga* is the modified Galileo number, defined as $Ga = \rho\sigma^3/(g\mu^4)$.

The Weber number (*We*) is defined as $We = \rho_l u_{\mathrm{Nu}}^2 \delta_{\mathrm{Nu}}/\sigma_l$ [2]. The methods for the pressure discretization and the pressure–velocity coupling are PRESTO and PISO, respectively. The second-upwind scheme was chosen to discretize the momentum and energy equations. In order to better analyze the effect of physical properties, four fluids listed in Table 1 are selected for comparative study, namely water, seawater, propane (R290), and liquid oxygen (O_2). The Kapitza number is defined as $Ka = \sigma(\rho/(\mu^4 g))^{1/3}$, which only reflects the physical properties of fluids. The *Ka* number is an important parameter that influences the film stability and wettability [35,36]. For better comparison, the *Ka* numbers of the four fluids are relatively close to each other.

Table 1. Properties of fluids.

Fluid	Condition	Density ρ/kg·m^{-3}	Dynamic Viscosity μ/μPa·s	SurfaceTension Coefficientσ/mN·m^{-3}	*Pr*	*Ka*
Water	T_{in} = 37 °C, p_s = 0.1 MPa	993	691	70	4.62	5344
Seawater	T_{in} = 50 °C, $S = 10^5$ g·kg^{-1}, p_s = 0.1 MPa	1066	712	71.5	4.15	5365
R290	T_{in} = −30 °C, p_s = 3.8 MPa	571	179	14	3.27	5391
O_2	T_{in} = −186 °C, p_s = 0.2 MPa	1158	214	14	2.32	5373

The wetting ratio (*WR*) is defined as $\mathrm{WR} = A_w/A$, where A_w and A refer to the wetting area and the bottom plate wall, respectively. The local heat transfer coefficient h is defined as $h = q/\Delta T$, where q and ΔT ($= T_w - T_{\mathrm{in}}$) refer to the local wall heat flux and temperature difference, respectively. T_w and T_{in} refer to the wall temperature and liquid inlet temperature, respectively. For heating conditions, the wall temperature is constant, based on ΔT = 5 °C when the liquid inlet temperature is certain. Considering the

fluctuation of film flow, all the film thickness and heat transfer coefficients are calculated by the time-average method.

The models' accuracy is validated in our previous work [2–4], which indicates that the present models simulate the local film thickness and local heat transfer coefficients with high accuracy.

3. Results

3.1. Falling Film Characteristics on the Smooth Plate

Figure 2 shows the local film thickness on the 2D smooth plate under different fluids. The result of the experiment using water (T_{in} = 25 °C) in [2] is selected for comparison. For the water (T_{in} = 25 °C), the local film thickness slightly decreases at first with the flow direction, then gradually increases, and finally reaches a stable value. However, the results of the other fluids decrease all the way, and gradually stabilize in the end. This is because the water has a higher viscosity when the liquid temperature decreases. Based on Nusselt's correlation of film thickness, as shown in Equation (7) [37], we obtain Nusselt's results of film thickness for water at T_{in} = 25 °C and T_{in} = 37 °C of 0.439 mm and 0.372 mm, respectively. As the length of the liquid inlet is fixed at 0.4 mm, this results in different variation trends along the flow direction for the two water cases. Figure 2 also depicts the film thickness results of Nusselt's correlation. It shows that all the final results of local film thickness are close to Nusselt's results, and the maximum relative deviations are within ±6.3%. We find that the final film thickness is positively correlated with the kinematic viscosity, which agrees with Nusselt's formula.

$$\delta_{Nu} = (3\mu_l Q/(\Delta\rho g W \sin\phi))^{1/3} \quad (7)$$

where δ_{Nu} represents the Nusselt film thickness, $\Delta\rho$ represents the density difference $\Delta\rho = \rho_l - \rho_g$, $Q = (Re\mu W/(4\rho))$ refers to the volume flow rate, and W is the plate width of the 3D models.

Figure 3 shows the local heat transfer coefficients for different fluids. We note that all the h results decrease with the flow direction, which is related to the development of the thermal boundary layer. In addition, the two water cases and the seawater case have close h results, and the maximal deviations are within ±1.3%. Compared with the above three fluids, the h results of the liquid oxygen are less, and those of the R290 are minimal. In the present study, we define the nominal thermal resistance as $R_{cond} = \delta_{avg}/\lambda$, where δ_{avg} refers to the average film thickness, and λ refers to the liquid thermal conductivity. The water (T_{in} = 25 °C) case is defined as the reference case, thus, λ_{25}, R_{25} ($R25 = \delta_{25}/\lambda_{25}$), $\delta_{25,}$ and h_{25} are the thermal conductivity, nominal thermal resistance, average film thickness, and average heat transfer coefficient, respectively, of the reference case. In addition, we observe that the liquid oxygen case has larger h than the R290 case, which infers the heat transfer coefficients of falling film flow are not linearly related to the Prandtl number.

The dimensionless results of λ/λ_{25}, δ_{avg}/δ_{25}, h_{avg}/h_{25}, and R_{cond}/R_{25} of the four fluids are shown in Figure 4. Although the δ_{avg} of water (T_{in} = 37 °C) and seawater are larger than those of the R290 and the liquid oxygen, the former cases have higher average heat transfer coefficients h_{avg} than the latter cases. This is because the former two fluids have higher thermal conductivity, which results in lower nominal thermal resistance. The above results show that an inverse relationship exists between the average heat transfer coefficient and the nominal thermal resistance, which infers the heat conduction greatly influences the sensible heat transfer of film flow.

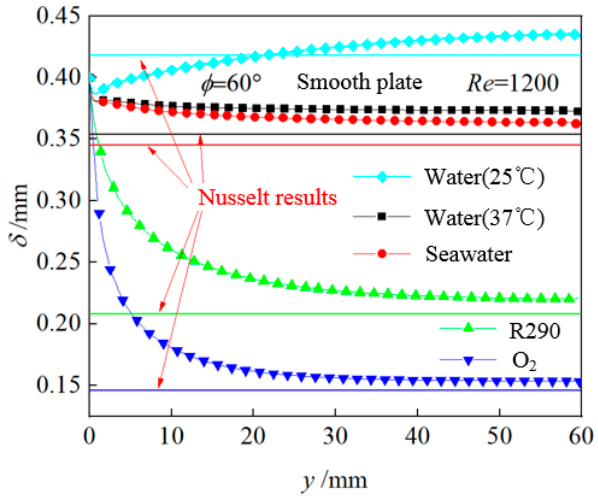

Figure 2. Local film thickness δ variation with y for different fluids.

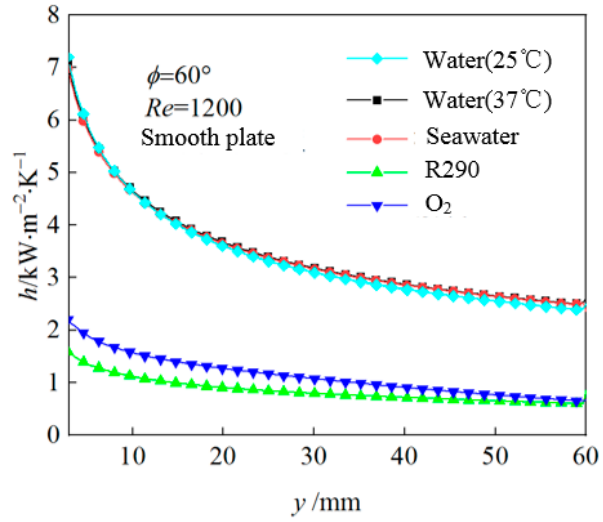

Figure 3. Local heat transfer coefficient h versus y for different fluids on the smooth plate.

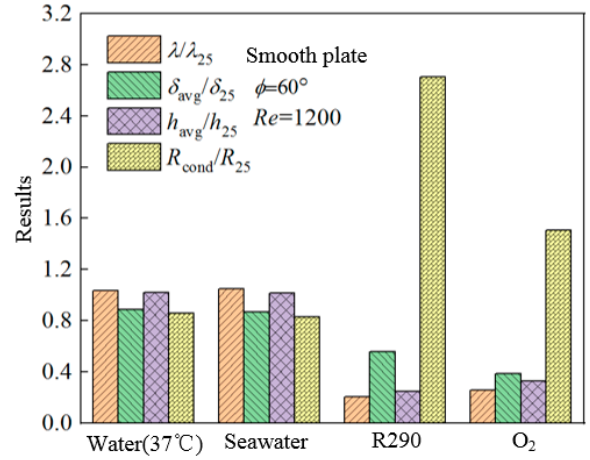

Figure 4. Dimensionless results for different fluids on the smooth plate.

Figure 5 shows the film distribution of four fluids on the smooth plate at We = 0.76, ϕ = 60°, and the left scale depicted in different colors reflects the film thickness. For the

four cases, all the film contracts into one main stream in the middle, and two minor streams flow on two sides. We define two points in this process, namely, the contraction point and the intersection point, as shown in Figure 5a. From the left to the right cases, the position of the contraction point gradually moves upward, and the main stream width behind the intersection point gradually narrows. The *WR* results of water, seawater, R290, and O_2 cases are 0.57, 0.56, 0.47, and 0.43, respectively. Lyu et al. [38] point out the higher surface tension goes against the film spreading, while higher dynamic viscosity has a conducive effect. The water and the seawater have nearly equal wettability, due to their similar physical properties. Moreover, they have large surface tension coefficients and dynamic viscosity coefficients, which are 5.0–5.1 and 3.2–4.0 times greater those of R290 and liquid oxygen, respectively. As the *WR* results of the water and the seawater are greater than those of the liquid oxygen and the R290, it infers that the viscosity force has a higher impact on film wettability than the surface tension.

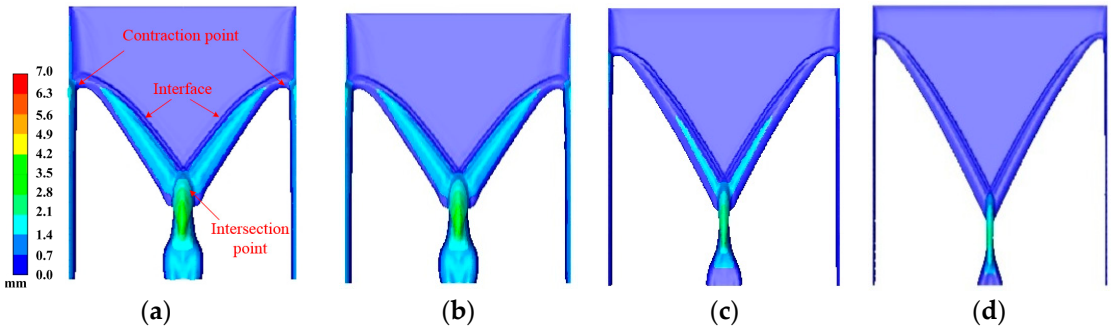

Figure 5. Film distribution and film thickness for different fluids: (**a**) water; (**b**) seawater; (**c**) R290; and (**d**) O_2.

The surface tension coefficients of R290 and liquid oxygen are similar, and the dynamic viscosity coefficient of liquid oxygen is greater than that of R290, while the *WR* of liquid oxygen is less than that of R290. This is because the kinematic viscosity of the liquid oxygen is smaller than that of the R290. The film flows more easily outside from the plate as the gravity force ($\rho g \cdot \sin\phi$) is larger, which can reduce the wetting area. It infers the film wettability mainly depends on the kinematic viscosity, rather than the dynamic viscosity. The larger the kinematic viscosity is, the better the film wettability is.

3.2. Falling Film Characteristics on the Corrugated Plate

Figure 6 shows the results of film surface position z for five fluids on the 2D triangular corrugated plate (Le = 5 mm, De = 0.7 mm). It notes that all the film surfaces fluctuate along the flow direction. The film surface positions of the R290 and the liquid oxygen are low, which are close to the shape of "triangular wave". The film surface positions of the other three fluids are higher, and the shapes are closer to the "sine wave". This is because the thinner film is more easily influenced by the wall structure, and the influence decreases when the distance between the film surface and the wall is further.

Figure 7 shows the local film thickness on the above triangular corrugated plate. The purple line in the bottom represents the wall position. Similar to the film surface position, the local film thickness also fluctuates along the flow direction. For the water (T_{in} = 25 °C), unlike the "sine wave" shape for the film surface position, the shape of film thickness is similar to the "triangular wave", and the maximum amplitude reaches about 0.4 mm. However, the film thickness results of the other fluids show quite different periodic variations. The film thickness of the liquid oxygen has the smallest fluctuation amplitude of 0.05 mm. Similar to the results on the smooth plate, the δ results of the R290 and the liquid oxygen decrease along the flow direction, while the δ results of the other fluids increase slightly, which indicates that the corrugated wall structure affects the film developmental process. This is because the distortive force produced by the corrugated

ribs hinders the film from spreading downwards. In addition, the viscosities of the waters and the seawater are larger than the other fluids, which intensifies the film accumulation on the wall. However, the liquid oxygen and the R290 have relatively smaller viscosity, and the distortive force and the viscous force are less than the gravity force, which results in the decrease in film thickness.

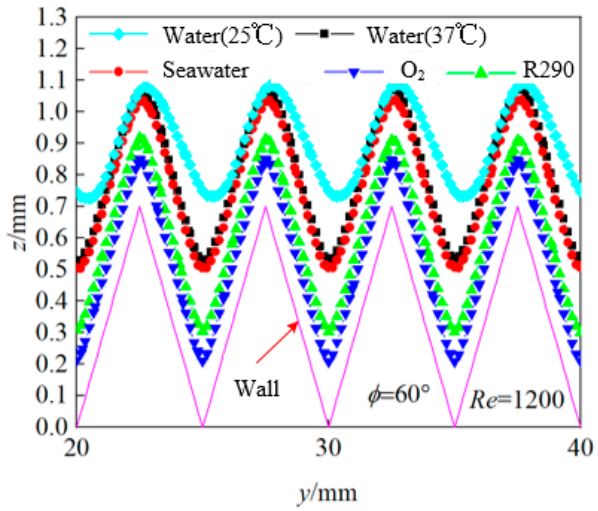

Figure 6. Film surface position z for different fluids.

Figure 8 shows the film streamline distributions of five fluids near y = 30 mm. Vortices exist in the wall trough regions for the water (T_{in} = 25 °C) case, while no vortex is found for the other fluids. Furthermore, we also find that vortices also occur under the water (T_{in} = 10 °C) case in the CFD method. As the water viscosity decreases with temperature, it infers that the viscosity also affects the occurrence of vortices in addition to the corrugation steepness ($St = De/Le$) [2]. The vortex tends to happen more easily when the liquid has a higher viscosity, because the viscous force hinders the film from flowing downwards, and more film is impeded at wall troughs. Finally, the vortices occur under the drag force caused by the upper flowing film.

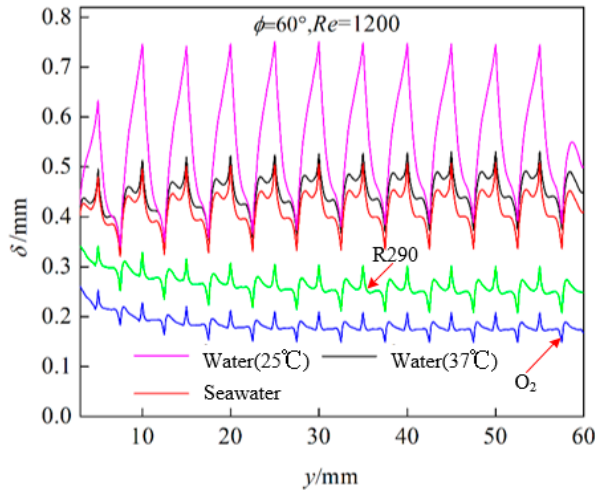

Figure 7. Local film thickness δ for different fluids.

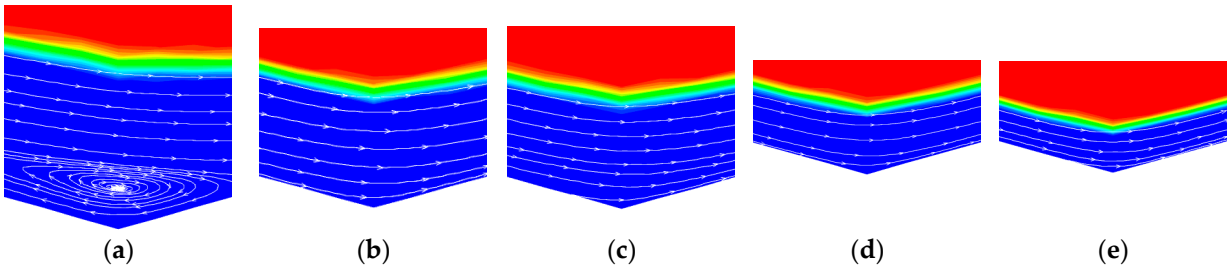

Figure 8. Streamline on the triangular corrugated plate for different fluids: (**a**) water (T_{in} = 25 °C); (**b**) water (T_{in} = 37 °C); (**c**) seawater; (**d**) R290; and (**e**) O_2.

Figure 9 shows the local heat transfer coefficients on the above triangular corrugated plate. It is found that the local heat transfer coefficients of all fluids decrease along the flow direction, and the fluctuation amplitudes decrease gradually. The water (T_{in} = 25 °C) case has the maximal fluctuation amplitude, which results from the large fluctuation in local film thickness. We also take the result of the water (T_{in} = 25 °C) as the reference case, and STD_{25} is defined as the global standard deviation of local film thickness for the reference case [2]. The dimensionless results of δ_{avg}/δ_{25}, STD/STD_{25}, h_{avg}/h_{25}, and R_{cond}/R_{25} are shown in Figure 10. Although the water (T_{in} = 37 °C) and the seawater cases have lower nominal thermal resistance than the reference case, the average heat transfer coefficients are close to the reference case. This is because the vortices generated at the wall trough enhance heat transfer for the reference case. The R290 and the liquid oxygen have lower heat transfer coefficients, due to their higher nominal thermal resistance.

Figure 11 shows the film distributions of the four fluids on the 3D triangular corrugated plate (*Le* = 6 mm, *De* = 0.6 mm). The left scale represents the film surface position *z*. Similarly, the positions of the contraction point rise gradually from left to right in each case. The *WR* results of the water, seawater, R290, and liquid oxygen cases are 0.53, 0.53, 0.47, and 0.40, respectively. The water and the seawater have the largest *WR*, followed by the R290, and the smallest is the liquid oxygen, which is consistent with the trend on the smooth plate. The difference compared with the results on the smooth plate is the wavy gas–liquid interfaces, which is affected by the corrugated wall.

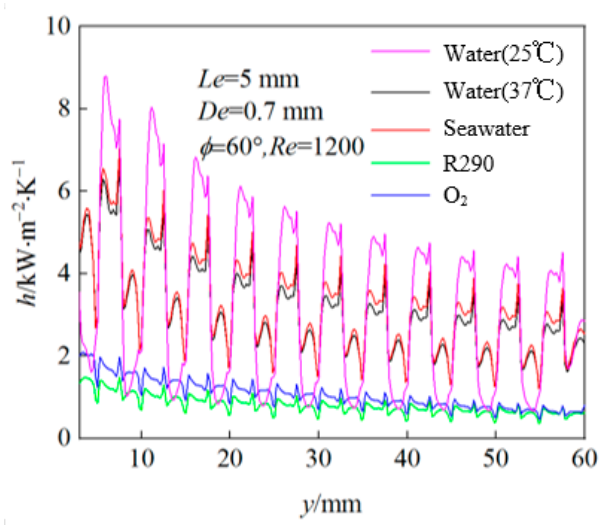

Figure 9. Local heat transfer coefficient *h* for fluids on the triangular corrugated plate.

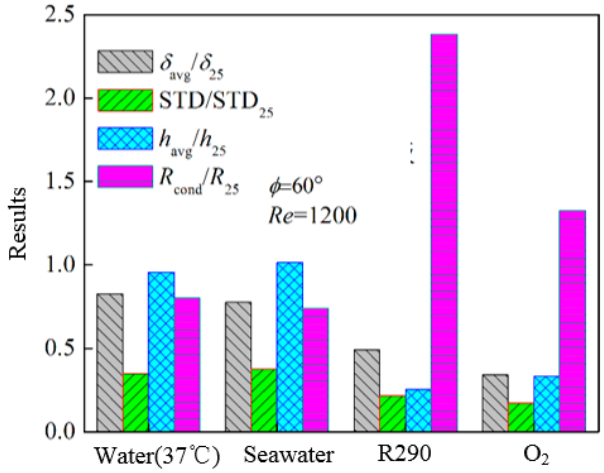

Figure 10. Dimensionless results on the triangular corrugated plate.

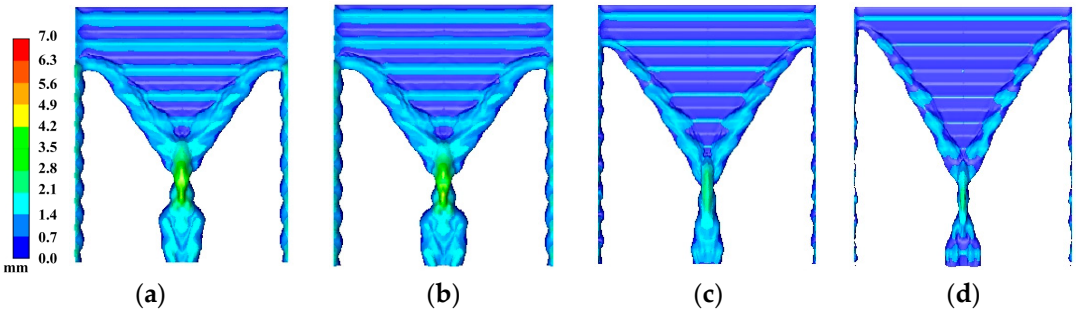

Figure 11. Film distribution for different fluids (We = 0.76, ϕ = 60°): (**a**) water; (**b**) seawater; (**c**) R290; and (**d**) O_2.

3.3. Falling Film Characteristics on the Round Tube

Figure 12 shows the local film thickness of the four fluids on a horizontal round tube. The local film thickness of the seawater is slightly lower than that of the water, followed by the R290, and the liquid oxygen. An evident increase in film thickness exists near the bottom region. For the water and the seawater cases, the results of local film thickness increase by 75.2% and 67.9%, respectively, at θ = 160–175°. Meanwhile the increases in the R290 and the liquid oxygen cases are only 18.9% and 11.2%, respectively. This is because the water and the seawater have higher viscosity, which results in more liquid remaining on the bottom of the tube.

Figure 13 shows the local heat transfer coefficients on the round tube. The local heat transfer coefficients of the water and the seawater are very close to each other, but greater than those of the R290 and the liquid oxygen. The h results decrease by 36.6%, 33.3%, 41.6%, and 72.1% at θ = 0–5° for the water, seawater, R290, and liquid oxygen, respectively, which is due to the impact of vortices forming on the top of the round tube. Similarly, the vortices produced by the film separation near the bottom of the tube (θ =175–180°) also intensify the heat transfer [3]. Average film thickness δ_{avg} is defined as the average value of local film thickness at all monitor points. By calculation, the nominal thermal resistances (δ_{avg}/λ) of the R290 and the liquid oxygen are 2.65 and 1.37 times that of the water, respectively. Thus, the cases of liquid oxygen and the R290 have lower heat transfer coefficients than those of the water case.

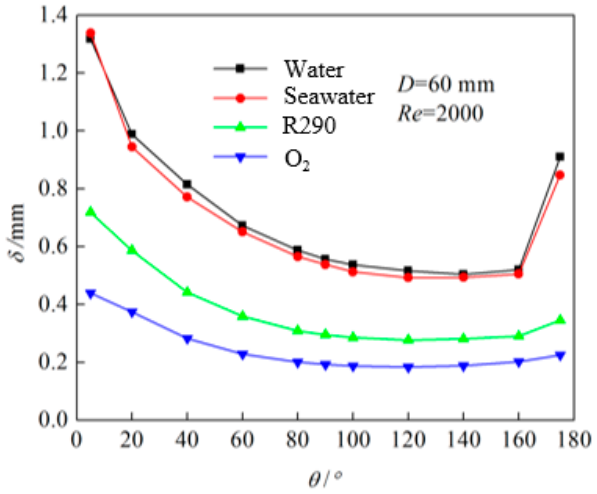

Figure 12. Local film thickness δ on the horizontal round tube.

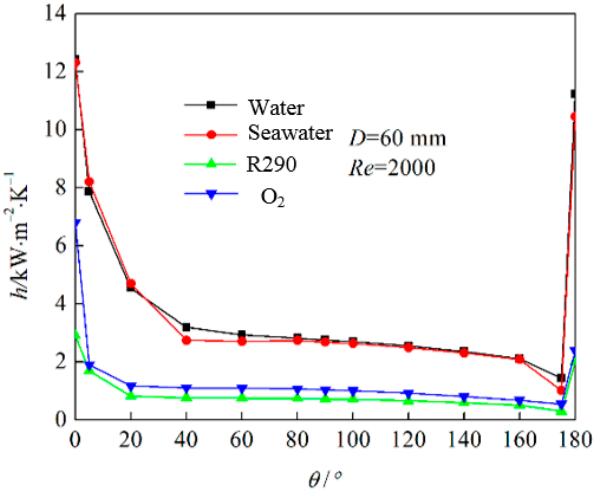

Figure 13. Local heat transfer coefficient h on the horizontal round tube.

Figure 14 shows the transient film thickness on the horizontal round tube under four different fluids. It clearly demonstrates that the film surfaces are unstable for the water, seawater, and R290 cases, while the liquid oxygen case has a nearly smooth film surface. The amplitudes of film thickness (almost 0.4 mm) for the water and the seawater are similar and large, and are greater than that of the R290. The film distributions on the horizontal round tube under four different fluids are shown in Figure 15. The film thickness results of the water and the seawater cases are evidently thicker than those of the R290 and the liquid oxygen. In addition, the prior two cases have wavier film surfaces, similar to a "teardrop", along the tube perimeter, which has a sharp downstream slope and a long gently sloping tail [39]. However, the latter two cases have relatively smoother surfaces, especially for the liquid oxygen case. The wavy film surfaces strongly depends on the liquid physical properties, namely, larger viscous force and gravity force, which contribute to the film stability, while larger surface tension has the opposite effect [40]. As seen in Table 1, both the dynamic viscosity and surface tension coefficients of the water and the seawater are larger than those of the other two cases. Thus, it infers that the influence of surface tension on the film stability is greater than that of the viscous force.

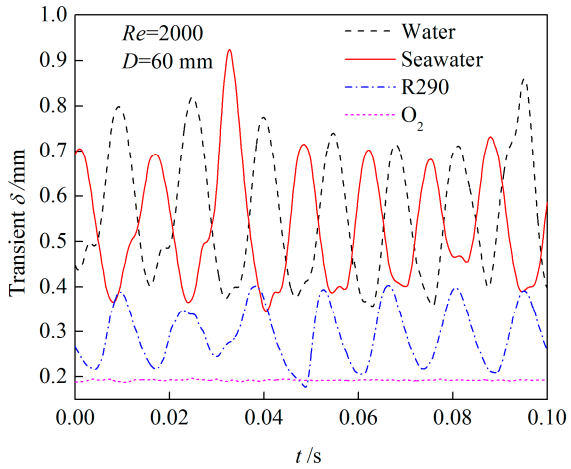

Figure 14. Transient film thickness on the horizontal tube.

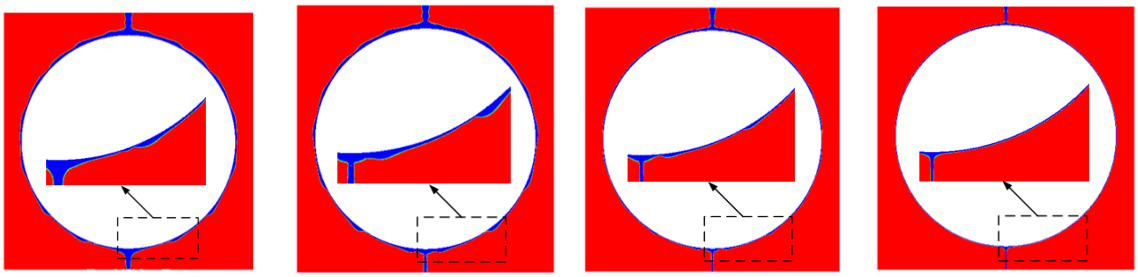

Figure 15. Film distribution on the horizontal tube under different fluids: (**a**) water; (**b**) seawater; (**c**) R290; and (**d**) liquid oxygen.

3.4. Falling Film Characteristics on the Elliptical Tube

Figure 16 shows the local film thickness of four fluids on the elliptical tube. It is found that the δ results of the water and the seawater at first gradually decrease by 36.0% and 40.8%, respectively, at θ = 5–160°. Subsequently, the results significantly increase by 16.1% and 18.6%, respectively, at θ = 160–175°. For the R290 and the liquid oxygen, the δ results decrease by 34.4% and 35.4%, respectively, at θ = 5–20°. Afterwards, they decrease slowly, and then increase by 2.9% and 3.2%, respectively, at θ = 160–175°; thus, their increased amplitudes of film thickness are lower than those of the water and the seawater at the tube bottom. Through comparison with results in Figure 12, the increases in local film thickness at the bottom of the elliptical tube are significantly less than those of the round tube. The reason for this is determined by the "thin and tall" shape of the elliptical tube. The film accelerates more easily with the gravity force and is separate from the wall, which leads to less film remaining on the bottom of the elliptical tube.

Figure 17 shows the local heat transfer coefficients on the elliptical tube. Similar to the results on the round tube, the local heat transfer coefficients are asymmetrically distributed along the tube perimeter, and change drastically at θ = 0–5° and 175–180°. The nominal thermal resistances of the R290 and the liquid oxygen are 2.92 and 1.53 times that of the water case, respectively, which results in lower heat transfer coefficients. It also infers that an inverse relationship exists between heat transfer coefficients and nominal thermal resistance.

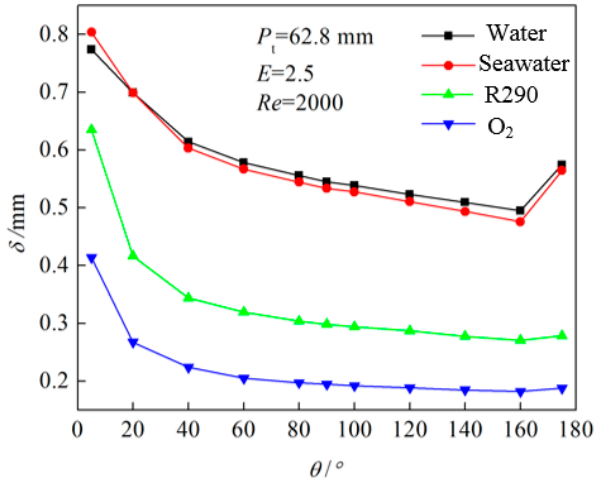

Figure 16. Local film thickness δ on the elliptical tube.

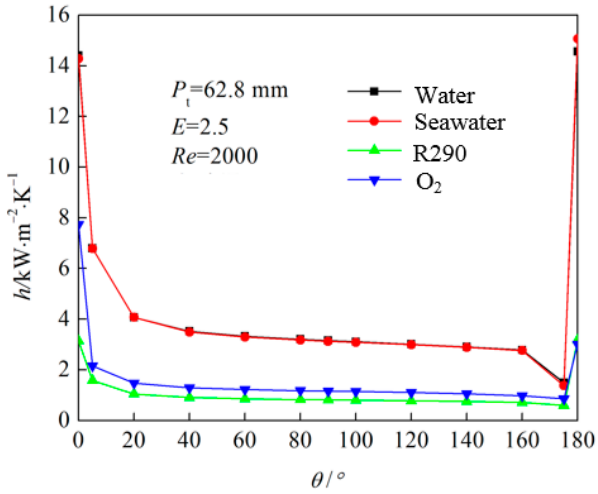

Figure 17. Local heat transfer coefficient h on the elliptical tube.

Figure 18 shows the film surfaces on the elliptical tube under four fluids. It indicates that the film surfaces are smoother than those on the round tube (see Figure 15). In addition, we observe that some liquid drops down from the film surface for the water and the seawater cases, while this does not happen for the same liquids on the round tube. This may be due to the greater acceleration effect brought by the gravity force on the elliptical tube, which results in a larger film velocity. Thus, there is not enough time for the film to grow sufficiently enough to be wavy [41,42]. When the film velocity is higher, the critical value, namely, the liquid inertial force, is larger than the adhesion force, then the liquid starts to detach from the film surface. Moreover, the film thickness results are thinner for the R290 and the liquid oxygen cases, and no droplets are observed, similar to those cases on the round tube. This is because the film velocity is still not high enough to overcome the effect of the adhesion force.

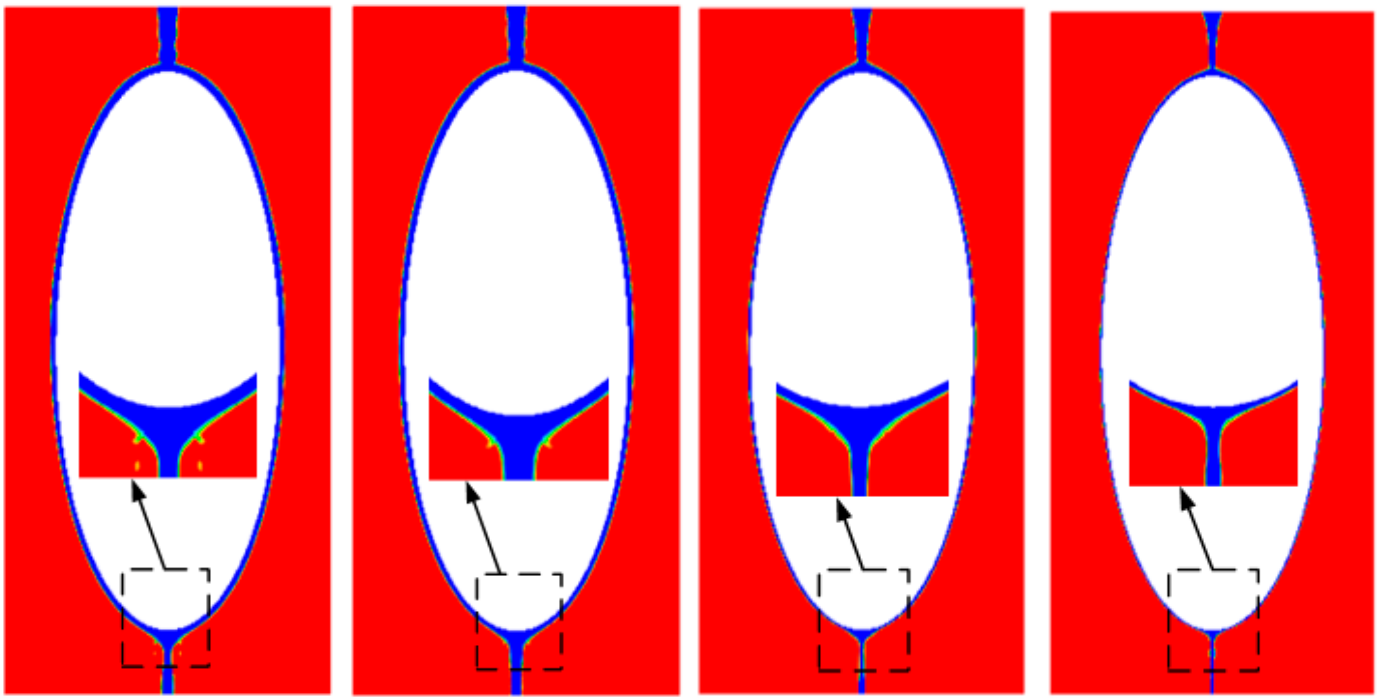

(**a**) (**b**) (**c**) (**d**)

Figure 18. Film distribution on the elliptical tube: (**a**) water; (**b**) seawater; (**c**) R290; and (**d**) O_2.

4. Conclusions

In this paper, the flow and heat transfer characteristics of falling film on different wall structures are explored. The studied fluids include water, seawater, R290, and liquid oxygen. The results of liquid film thickness, heat transfer coefficients, and wetting performance on four structures are compared. The main conclusions are as follows:

(1) The local heat transfer coefficients decrease gradually as film flows on the smooth plate. An inverse relationship exists between the average heat transfer coefficients and the nominal thermal resistance. The kinematic viscosity, rather than the dynamic viscosity, affects the film wettability, and the effect of kinematic viscosity is greater than that of surface tension. The wetting ratio increases with the kinematic viscosity. The film surface on the triangular corrugated plate is wavier than that on the smooth plate;

(2) On the triangular corrugated plate, the film surface presents a shape with periodic fluctuation. When the liquid film thickness is small, the film surface presents a "triangular wave" shape similar to the wall structure, but when the film thickness is large, the film surface is close to the "sine wave" shape. The local heat transfer coefficient and its fluctuation amplitude decrease gradually along the flow direction. The vortices are easier to produce when the film viscosity is higher;

(3) The surface tension has more influence on the film stability than the viscous force. Compared with the round tube, it is hard for the film to develop into a wavy surface on the elliptical tube. The local film thickness results of the water and the seawater increase more evidently near the bottom of the horizontal pipe than those of the R290 and the liquid oxygen. The rise of local film thickness on the bottom of the elliptical tube is less than that on the round tube. The local heat transfer coefficients decrease rapidly when θ = 0–5°, and finally increase sharply at θ = 175–180°.

Author Contributions: Funding acquisition, H.S.; Investigation, Z.W.; Project administration, Z.W.; Software, Z.W.; Supervision, Y.L.; Writing—original draft, Z.W.; Writing—review & editing, P.W. All authors have read and agreed to the published version of the manuscript.

Funding: The work was funded by the Doctor Foundation of Jiangxi University of Science and Technology (Grant No: 205200100598), and the Officials of the Jiangsu Housing and Urban and Rural Construction Project (Grant No: 2019ZD076).

Institutional Review Board Statement: Not applicable.

Informed Consent Statement: Not applicable.

Data Availability Statement: Not applicable.

Acknowledgments: Jiangsu Vocational Institute of Architectural Technology and Jiangxi University of Science and Technology are gratefully acknowledged.

Conflicts of Interest: The authors declare no conflict of interest.

Nomenclature

a	The semi-major axis of the ellipse (m)
b	The semi-minor axis of the ellipse (m)
c_p	Specific heat capacity ($J \cdot kg^{-1} \cdot K^{-1}$)
D	Round tube diameter (m)
E	Tube ellipticity (=a/b)
g	Gravity acceleration ($m \cdot s^{-2}$)
h	Local heat transfer coefficient ($W \cdot m^{-2} \cdot K^{-1}$)
Ka	Kapitza number (-)
sP_t	Half of the tube perimeter (m)
q	Heat flux ($W \cdot m^{-2}$)
Re	Reynolds number (-)
T_{in}	Liquid inlet temperature (°C)
T_w	Wall temperature (°C)
We	Weber number (-)
Greek letters	
Γ	Mass flow rate per unit length ($kg \cdot m^{-1} \cdot s^{-1}$)
α	Volume fraction (-)
θ	Peripheral angle (°)
σ	Surface tension coefficient ($N \cdot m^{-1}$)
δ	Local film thickness (mm)
λ	Thermal conductivity ($W \cdot m^{-1} \cdot K^{-1}$)
μ	Dynamic viscosity (Pa·s)
ρ	Density ($kg \cdot m^{-3}$)
Subscripts	
l	Liquid
g	Gas

References

1. Wen, T.; Lu, L.; He, W.; Min, Y. Fundamentals and applications of CFD technology on analyzing falling film heat and mass exchangers: A comprehensive review. *Appl. Energy* **2020**, *261*, 114473. [CrossRef]
2. Wan, Z.; Li, Y. Numerical study of the falling film wettability and heat transfer on the inclined plates with different corrugated structures. *Asia-Pacific J. Chem. Eng.* **2021**, *16*, e2664. [CrossRef]
3. Wan, Z.; Li, Y.; Wang, S. A comprehensive simulation and optimization on heat transfer characteristics of subcooled seawater falling film around elliptical tubes. *Appl. Therm. Eng.* **2021**, *189*, 116675. [CrossRef]
4. Wan, Z.; Li, Y. Refrigerant film flow and heat transfer characteristics on the elliptical tube under constant wall temperature. *Appl. Therm. Eng.* **2022**, *200*, 117669. [CrossRef]
5. Bustamante, J.G.; Garimella, S. Experimental assessment of flow distributors for falling-films over horizontal tube banks. *Int. J. Refrig.* **2019**, *101*, 24–33. [CrossRef]
6. Chen, X.; Wang, J.; Lu, T.; Sheng, J.; Chen, X. Three-dimensional film thickness distribution of horizontal tube falling film with droplet and sheet flow. *Int. J. Multiph. Flow* **2022**, *148*, 103933. [CrossRef]
7. Chen, J.; Zhang, J.; Ma, Z. Falling film mode transitions on horizontal enhanced tubes with two-dimensional integral fins: Effect of tube spacing and fin structures. *Exp. Therm. Fluid Sci.* **2019**, *101*, 241–250. [CrossRef]
8. Zheng, Y.; Chen, G.; Zhao, X.; Sun, W.; Ma, X. Falling liquid film periodical fluctuation over a superhydrophilic horizontal tube at low spray density. *Int. J. Heat Mass Transf.* **2020**, *147*, 118938. [CrossRef]

9. Hong, S.J.; Wang, E.S.; Park, C.W. Heat transfer characteristics of falling film and pool boiling evaporation in hybrid evaporator in vapor compression system. *Appl. Therm. Eng.* **2019**, *153*, 426–432. [CrossRef]
10. Cao, C.; Xie, L.; Du, Y.; Zhu, X.; Zhang, W. Three-Dimensional Flow Behavior of a Falling Film on Horizontal Tubes: A Comparative Study on Smooth and Finned Tubes. *Ind. Eng. Chem. Res.* **2022**, *61*, 2346–2358. [CrossRef]
11. Zhang, H.; Zhou, Y. Effect of wind speed on the spatial distribution of liquid film thickness outside the horizontal falling-film tube. *Int. J. Heat Mass Transf.* **2022**, *187*, 122584. [CrossRef]
12. Guo, Y.; Bao, M.; Gong, L.; Shen, S.; Zhang, K. Numerical investigation of the falling film thickness and heat transfer characteristics over horizontal round tube. *Int. J. Multiph. Flow* **2022**, *149*, 103977. [CrossRef]
13. Zhao, C.-Y.; Yao, Z.-L.; Qi, D.; Ji, W.-T.; Li, A.-G.; Tao, W.-Q. Numerical investigation of tube bundle arrangement effect on falling film fluid flow and heat transfer. *Appl. Therm. Eng.* **2022**, *201*, 117828. [CrossRef]
14. Karmakar, A.; Acharya, S. Numerical simulation of falling film sensible heat transfer over round horizontal tubes. *Int. J. Heat Mass Transf.* **2022**, *190*, 122727. [CrossRef]
15. Mao, N.; Hao, J.; He, T.; Xu, Y.; Song, M.; Tang, J. Unsteady heat transfer properties of spray falling over a horizontal tube in an oily sewage source heat pump. *Appl. Therm. Eng.* **2020**, *179*, 115675. [CrossRef]
16. Mao, N.; Hao, J.; Xu, Y.; Song, M.; Tang, J. A numerical study on non-uniform characteristics of spray falling heat transfer over horizontal tubes in an oily sewage source heat pump. *Int. J. Heat Mass Transf.* **2020**, *154*, 119679. [CrossRef]
17. Tahir, F.; Mabrouk, A.; Koç, M. CFD analysis of falling film hydrodynamics for a lithium bromide (LiBr) solution over a horizontal tube. *Energies* **2020**, *13*, 307. [CrossRef]
18. Álvarez, M.; Bourouis, M. Modelling of Coupled Heat and Mass Transfer in a Water-Cooled Falling-Film Absorber Working with an Aqueous Alkaline Nitrate Solution. *Energies* **2021**, *14*, 1804. [CrossRef]
19. Huang, K.; Hu, Y.; Deng, X. Experimental study on heat and mass transfer of falling liquid films in converging-diverging tubes with water. *Int. J. Heat Mass Transf.* **2018**, *126*, 721–729. [CrossRef]
20. Eichinger, S.; Storch, T.; Grab, T.; Tepel, S.; Heinrich, M.; Fieback, T.; Gross, U. Heat transfer and wetting behaviour of falling liquid films in inclined tubes with structured surfaces. *Appl. Therm. Eng.* **2022**, *205*, 118023. [CrossRef]
21. Wang, J.; Hu, Z.; Dong, H.; Zeng, S.; Bai, L.; Zhang, X.; Wang, Y. Experimental study on hydrodynamics of ionic liquids systems in falling film evaporator. *Chem. Eng. Process. Process Intensif.* **2022**, *170*, 108701. [CrossRef]
22. Li, H.; Yi, F.; Li, X.; Pavlenko, A.N.; Gao, X. Numerical Simulation for Falling Film Flow Characteristics of Refrigerant on the Smooth and Structured Surfaces. *J. Eng. Thermophys.* **2018**, *27*, 1–19. [CrossRef]
23. Jourdan, N.; Kanniche, M.; Neveux, T.; Potier, O. Experimental Characterization of Liquid Flows in Cooling Tower Packing. *Ind. Eng. Chem. Res.* **2022**, *61*, 2926–2936. [CrossRef]
24. Shi, Y.; Chen, G. Experimental study of falling film absorption with potassium formate—Water as working pair. *Int. J. Therm. Sci.* **2022**, *176*, 107520. [CrossRef]
25. Wei, J.; Liu, J.; Xu, X. Theoretical and Experimental Investigation of the Minimum Wetting Rate of a Falling Water Film on the Vertical Grooved Plate. *Ind. Eng. Chem. Res.* **2021**, *61*, 845–854. [CrossRef]
26. Pavlenko, A.N.; Volodin, O.A.; Surtaev, A.S. Hydrodynamics in falling liquid films on surfaces with complex geometry. *Appl. Therm. Eng.* **2017**, *114*, 1265–1274. [CrossRef]
27. Zhou, Y.; Yu, J. Optimization design of falling film type plate-fin condenser/reboilers by minimizing specific entropy generation rate. *Cryogenics* **2019**, *99*, 25–31. [CrossRef]
28. Gu, C.; Zhang, R.; Zhi, X.; Zhu, S.; Qiu, L. Numerical investigation on the flow characteristics of liquid oxygen and water in the structured packing. *Cryogenics* **2020**, *110*, 103140. [CrossRef]
29. Brackbill, J.; Kothe, D.; Zemach, C. A continuum method for modeling surface tension. *J. Comput. Phys.* **1992**, *100*, 335–354. [CrossRef]
30. Toshihiko, F.; Tatsuhiro, U. Heat transfer to falling liquid films and film breakdown—II: Saturated liquid films with nucleate boiling. *Int. J. Heat Mass Transf.* **1978**, *21*, 97–108. [CrossRef]
31. Luo, Y.; Chen, Y.; Zhong, D.; Wang, Y.; Yang, H. Experimental study of the flow characteristics in a falling film liquid desiccant dehumidifier. *Sci. Technol. Built Environ.* **2017**, *23*, 157–165. [CrossRef]
32. Tailby, S.; Portalski, S. Wave inception on a liquid film flowing down a hydrodynamically smooth plate. *Chem. Eng. Sci.* **1962**, *17*, 283–290. [CrossRef]
33. Hu, X.; Jacobi, A. The Intertube Falling Film: Part 1—Flow Characteristics, Mode Transitions, and Hysteresis. *ASME J. Heat Transf.* **1996**, *118*, 616–625. [CrossRef]
34. Rogers, J.T.; Goindi, S.S. Experimental laminar falling film heat transfer coefficients on a large diameter horizontal tube. *Can. J. Chem. Eng.* **1989**, *67*, 560–568. [CrossRef]
35. Njifenju, A.K. Experimental investigation of liquid films in gravity-driven flows with a simple visualization technique. *Exp. Fluids* **2013**, *54*, 1506. [CrossRef]
36. Lu, Y.; Stehmann, F.; Yuan, S.; Scholl, S. Falling film on a vertical flat plate—Influence of liquid distribution and fluid properties on wetting behavior. *Appl. Therm. Eng.* **2017**, *123*, 1386–1395. [CrossRef]
37. Nusselt, W. Die oberflachenkondensation des wasserdampfes. *Z. Ver. Dtsch. Ing.* **1916**, *60*, 541–575.
38. Lyu, Y.; Yin, Y.; Zhang, X.; Jin, X. Investigation of falling-film plate wettability characteristics under dehumidification and regeneration conditions using LiCl-H2O. *Int. J. Refrig.* **2018**, *94*, 118–126. [CrossRef]

39. Ramaswamy, B.; Chippada, S.; Joo, S.W. A full-scale numerical study of interfacial instabilities in thin-film flows. *J. Fluid Mech.* **1996**, *325*, 163–194. [CrossRef]
40. Young, G.W.; Davis, S.H. Rivulet instabilities. *J. Fluid Mech.* **1987**, *176*, 1–31. [CrossRef]
41. Gao, D.; Morley, N.; Dhir, V. Numerical simulation of wavy falling film flow using VOF method. *J. Comput. Phys.* **2003**, *192*, 624–642. [CrossRef]
42. Takamasa, T.; Hazuku, T. Measuring interfacial waves on film flowing down a vertical plate wall in the entry region using laser focus displacement meters. *Int. J. Heat Mass Transf.* **2000**, *43*, 2807–2819. [CrossRef]